Iqbal and Head
Advances in Bridge Engineering (2024) 5:30
https://doi.org/10.1186/s43251-024-00138-0

Advances in
Bridge Engineering

ORIGINAL INNOVATION Open Access

Parametric study for shear failure of bearing pads due to hurricane-induced wave loadings

Waqas Iqbal[1] and Monique Head[1*]

*Correspondence:
head@udel.edu

[1] Department of Civil and Environmental Engineering, University of Delaware, Newark, DE, USA

Abstract

The increasing frequency of extreme weather events, such as hurricanes and rising sea levels due to climate change, presents significant challenges to coastal infrastructure. With 42% of bridges in the United States exceeding 50 years of age, which surpasses their intended service life, there is a pressing need to assess their structural integrity, especially in coastal regions. This study focuses on evaluating the structural performance of bearing pads in coastal bridges under hurricane-induced wave loadings. Utilizing a combination of physics-based models (PBM), nonlinear modal time history analysis, and numerical validation, the research examines the hysteresis response of eight distinct bearing pad configurations. The findings indicate that reinforced circular bearing pads exhibit significantly greater shear displacements compared to plain elastomeric pads, underscoring the critical influence of shape factors on shear response. Fragility functions developed in the study illustrate the probability of shear failure, with reinforced circular pads showing a 28% higher likelihood of exceedance compared to rectangular plain pads. These results highlight the necessity for advanced design methodologies specifically for bearing pads to enhance the resilience of coastal infrastructure against severe hydrodynamic forces induced by hurricanes.

Keywords: Coastal bridges, Bearing pads, Hydrodynamic loads, Hysteresis loops, Nonlinear modal time history analysis, Fragility functions, Shear displacements

1 Introduction

Coastal infrastructure, particularly bridges, face heightened vulnerability to climate change and intensified natural hazards such as coastal storms, hurricanes, and rising sea levels. Sea level rise projections indicate a rise in flood elevations due to global warming, with estimates suggesting increases of 0.3 to 0.8 m by the 2030s and 2080s (Mousavi et al. 2011). Due to sea-level rise (SLR) and climate change, frequency and intensity of hurricanes have increased over the east coast which is posing threats to coastal infrastructure. The severe effects of climate change, like coastal storms, can also pose threats to life safety and bridge infrastructure (Boin and McConnell 2007). Storm surges and waves during coastal storms and hurricane events exert significant vertical and horizontal forces, posing challenges for low-clearance bridges originally designed without considering such loads (Mondoro et al. 2017). With increased demands, structures are also deteriorating with time as the American Society of Civil Engineers (ASCE) identified

one in thirteen (7.5% of all nation bridges as structurally deficient, which has necessitated an estimated investment of $125 billion to address deficiencies and bridge repair works (ASCE 2021).

Design codes have evolved over the last three decades to enhance structural resilience and incorporate new loading conditions as shown in Fig. 1 (Iqbal et al. 2023). ASCE standards have included flood loadings since 1995, with subsequent revisions addressing flood-resistant design requirements (Ingargiola et al. 2013; FEMA 2021). The Federal Emergency Management Agency (FEMA)'s publication of FEMA P-55 provided guidelines for coastal structure design to mitigate economic losses from hazards (FEMA 2011). The American Association of Highway and Transportation Officials (AASHTO and LRFD 2020) offered detailed specifications for bridges vulnerable to coastal storms reflected in the International Building Code (IBC 2018). Despite the evolution of design codes, there are still some gaps in the design approach. A research study conducted by (Moeini and Memari 2023) noted differences in hydrodynamic forces on residential buildings between experimental measurements and equations in (ASCE 7 2016) standards. Recently, ASCE has published its Supplement 2 for (ASCE 7, 2022) standard, including SLR projections to determine design flood elevation, scale factors corresponding to mean recurrence interval, and risk categories that calculate the still water elevation. The flood hazard area has also increased from a 100-year flood plain to a 500-year flood plain for risk categories II, III, and IV to improve the performance of structures subjected to flood loadings (ASCE, 2023). Tomiczek et al. (2019) noted that code-prescribed assumptions (including depth-limited wave height and the choice of dynamic pressure coefficient based on building risk category) could overestimate wave-induced forces by a factor of 20 compared to the measured forces.

Probabilistic assessment and performance-based design are recommended when analyzing structures subjected to unexpected loadings due to extreme hazards like hurricanes, earthquakes, wind, tsunamis, fire, and blast loadings. For the first time in history, the Applied Technology Council (ATC) adopted a performance-based earthquake engineering methodology that involved the fragility function calculation using parameters like intensity measure, damage states, and engineering demand parameters (Porter et al. 2007). This framework was adopted in the wind engineering community (PBWE) by

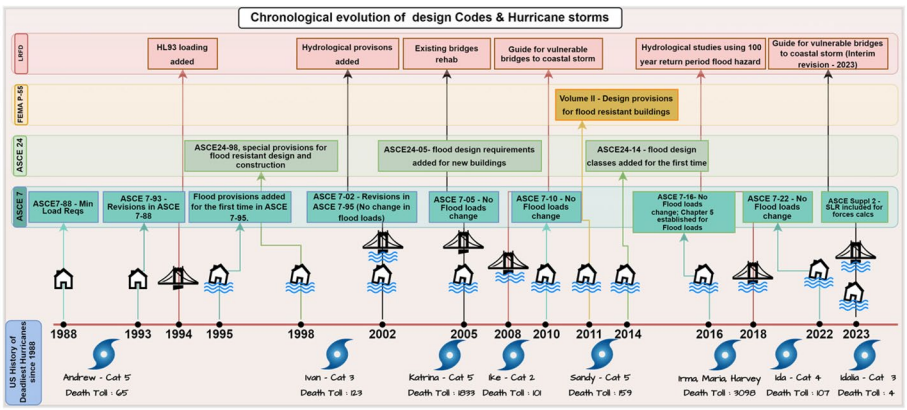

Fig. 1 The chronological evolution of design codes and hurricane storms

(Ciampoli et al. 2011), tsunamis (PBTE) by (Attary et al. 2017, 2019), and hurricanes (PBHE) by (Barbato et al. 2013). Ciampoli et al. (2011) provided a comprehensive presentation of the probabilistic procedure for applying Performance-Based Design concepts to wind engineering that were then demonstrated through a case study, which assessed both the failure probability (fragility) due to flutter instability and the out-of-service risk of a bridge design based on the preliminary design of the suspension bridge over the Messina Strait in Italy. Attary et al. (2017, 2019) proposed a probabilistic Performance-Based Tsunami Engineering (PBTE) framework, based on the total probability theorem for assessing the risk of structures exposed to tsunamis. This framework breaks down the analysis into distinct phases: hazard analysis, foundation and structure characterization, interaction analysis, structural analysis, damage analysis, and loss analysis. Barbato et al. (2013) introduced an innovative fully probabilistic Performance-Based Hurricane Engineering (PBHE) framework for assessing the risk of structural systems in hurricane-prone regions by considering the effects and interactions of wind, flood, windborne debris, and rainfall. These frameworks use the theorem of total probability, breaking down joint distributions into smaller parts to calculate the overall probability of the decision variable.

Performance-based design methodologies have also been implemented for specific types of coastal structures (Van de Lindt and Dao 2009; Van de Lindt and Taggart 2009; Do et al. 2016; Attary et al. 2017; Cui and Caracoglia 2018) by leveraging fragility functions and evaluation of mitigation strategies. Do (2016) used the fluid-structure interaction approach to quantify forces on elevated structures specifically for bridges and developed fragility curves for four different bridge elevations. The fragility analysis of coastal bridges under wave forces can provide engineers with valuable insights into the vulnerability of the structures and implement modified design code practices. Shoji and Moriyama (2007) evaluated the structural fragility of a coastal bridge due to the 2004 tsunami in Indonesia, and the relation between the damage probability and tsunami wave parameters was obtained. Ataei et al. (2010) built a finite element (FE) model for a T-girder bridge to assess the vulnerability under various hurricane conditions, and the significance of wave parameters was evaluated. Most of the wave-induced damages are attributed to the failure of connections between the superstructures and substructures. Bridge damage due to connection failure is inevitably accompanied by rubber shearing, sliding on the contact surface, bearing unseating, and the excessive stress of the upper and lower plates. Targeting the unseating failure model, (Ataei and Padgett 2013) presented a methodology to derive fragility surfaces for coastal bridges by comparing the structural capacity with the total uplift force to overcome the unseating failure. Similarly, (Xu et al. 2022) analyzed the failure mechanism of the typical coastal box-girder bridges with LRBs under wave forces, and the failure modes such as the deck unseating, sliding, and bearing shearing were discussed. In a research study conducted by (Rahman and Billah 2023), it was observed that deck-level loadings caused a high probability of exceedance compared to the pier-level loadings because the high fragility of the substructure-superstructure connection resulted in the unseating of bridge decks. Huang et al. (2019) analyzed the failure probabilities of simply supported box-girder bridges with connection types of direct contact and the laminated rubber bearing (LRB), and the other four connections were further studied by (Huang et al. 2022). For this study, a

similar approach from the PBHE framework proposed by (Huang et al. 2022) is used to analyze eight distinct bearing pad configurations for shear resistance due to hurricane-induced lateral wave forces and developing fragility functions for single-side bonded elastomeric rubber pads due to five distinct wave time histories.

2 Research background

In the past, there have been enormous research studies focusing on the performance of typical connections under a series of quasi-static and cyclic wave forces. Guo et al. (2015) performed a hydrodynamic experiment focused on studying wave forces on coastal highway bridges. The experiment used a full-scale bridge model that included the superstructure, substructure, and adjacent segments. It investigated both quasi-static and slamming components of vertical wave forces, as well as horizontal wave forces under varying conditions of clearance, wave height, and wave period. The study compared experimental results with theoretical models proposed by Douglass and AASHTO guidelines to validate these models. Lehrman et al. (2012) conducted a full-scale experimental test to investigate the performance of three commonly used connections for AASHTO Type III prestressed concrete girders to deck slab under hurricane wave forces. Then, a series of static and dynamic analyses were performed to study the response of the anchor bolt or clip-bolt enhanced connection. It was observed that no anchorage type was sufficient for significant wave heights due to entrapped air within girders. Saeidpour et al. (2019) introduced a method for assessing the structural vulnerability of simply supported coastal bridges to hurricanes, aiming to enhance their resilience against severe weather events like hurricanes Ike, Katrina, and Ivan. The methodology addressed uncertainties related to hurricane hazards and bridge responses by establishing probability distributions, particularly considering extreme wave heights and periods using wave spectral density. The method was applied successfully to coastal bridges in Georgia, USA, demonstrating its capability to probabilistically model demands, capacities, and hazards. Overall, the study highlighted the potential of this framework for identifying and ranking the bridges most susceptible to hurricane impacts.

Bearing pad geometry and bonding has a significant effect on hysteresis response of bearing pads. A study by (Krahl et al. 2020) presented an analytical method for predicting the nonlinear moment-rotation relationship between bearing pads and precast beams, emphasizing the significance of geometry in determining rotational stiffness. According to a study conducted by (Xiang and Li 2018), fully bonded elastomeric bearings led to smaller shear displacements compared to fully unbonded bearing pads. This is attributed to bonding facilitating the full utilization of shear stiffness in the bearings, effectively restraining lateral displacement. Xiang and Li (2016) also performed quasi-static tests to experimentally investigate the cyclic behavior of top-side bonded bridge elastomeric bearings under lateral loads, as demonstrated in Fig. 2a, that is used in this research study to compare with the dynamic response using the analytical and numerical models.

Different modeling approaches when performing numerical analyses have been shown to influence the response and therefore the results when understanding the effects of bearing pad performance when subjected to lateral loads. Considering the

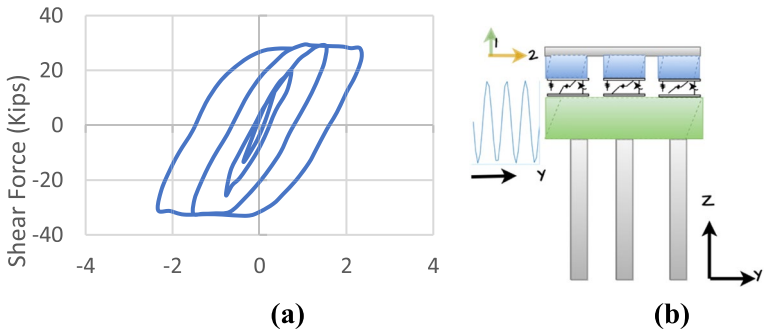

Fig. 2 **a** Hysteresis response of plain elastomeric bearing pad (Xiang and Li 2016). **b** Failure schematic of the typical bearing pad due to shear forces induced from wave loadings

impact of both full bonding and full unbonding of bearing contact surfaces on bridge performance, (Xiang et al. 2021) suggest employing a single-side bonded installation method for elastomeric bearings by modeling the flexible moment connection between girder soffit and bent beam/pier cap, expected to offer superior performance. Single-side bonded bearings exhibit a constrained shear stress response, bounded by the sliding frictional force at the unbonded surface, thereby providing an isolated reaction for the bridge substructure. Moreover, their response is more stable compared to fully bonded bearings, mitigating tendencies for rolling over due to restraints of curling deformations. The behavior of single-side bonded elastomeric bearings falls between fully bonded and unbonded bearings, demonstrating an elastic-perfectly-plastic response to lateral force-displacement. Conversely, bonding the top and bottom surfaces of bearings generates local tensile stress, potentially leading to damages such as delamination and rubber tearing. Unbonded methods, however, effectively release local tensile stress by generating lift-off deformations. Additionally, using unbonded strategies isolates superstructure rotation-induced bending moments from transmitting to the substructure, akin to shear force. To understand the bearing pad failure mode due to shear displacements, Fig. 2b illustrates the mechanism of connection failure, wherein displacements arising from lateral wave loading contribute to the failure of connections. Shear failure could result in the tearing of the pad hence leading to the instability of bearing pads. This instability could cause the girder's displacements and along with buoyant forces induced by hydrostatic forces cause the deck lift and displacement. Due to the dynamic and cyclic nature of wave loading, connection behavior can be better predicted by energy dissipation and residual displacements The hysteresis response of bearing pads has been extensively studied through experimental and numerical simulations due to seismic activities. However, there remains a gap in research regarding the hysteresis response of bearing pads specifically due to hurricane-induced wave loading. This study aims to fill this gap by conducting a parametric study to evaluate the hysteresis response of different bearing configurations under hurricane-induced lateral wave cyclic forces and develop fragility functions for bearing pads subjected to lateral wave loadings. The results provide insights into the potential vulnerability of bridges with these different bearing configurations if

subjected to various hurricane-induced wave loadings that are becoming more common due to the changing climate and extreme weather events.

3 Research methodology

This research methodology is focused on the comparative analysis of the shear response of eight distinct bearing pad configurations for quasi-static and dynamic forces. Shear response due to dynamic forces is captured by developing hysteresis curves resulting from cyclic wave time histories developed by linear wave theory. Monte Carlo simulations are used to generate two hundred wave time histories which are then narrowed down to five distinct wave time histories using wave energy density. Hysteresis loops are developed for all eight bearing pads for five distinct wave time histories. Similarly, shear response due to quasi-static forces utilized physics-based models adopted by the AASHTO coastal guide while considering factors such as girder height, and wave parameters like wave height and wave period. An analytical model of one span simply supported bridge is created with elastomeric bearings modeled as non-linear links between the superstructure and sub-structure. Fast Non-Linear analysis (FNA) is used to address computational effort and while acknowledging the validity of FNA for component level non-linearity. Both quasi-static and cyclic wave forces are applied laterally to the trailing edge of the bridge as suggested by the AASHTO coastal guide. Non-linear links with shear stiffness depending upon plastic wen material model and two distinct geometric approaches for plain and reinforced bearing pads respectively are used for modeling purposes. Plain elastomeric bearing pad's geometric properties are taken from basic mechanics, while reinforced pad's geometric properties are dependent upon shape factors (Hosseini, 2022). Due to the maximum shear displacements of elastomeric pads for time history with highest wave frequency and wave height, this wave time history is chosen for the finite element analysis and comparative analysis of bearing pad response for each modeling technique. A finite element model of a bridge abutment with an elastomeric pad is created while considering the Neo-Hooken hyperelastic material model for the bearing pad. For the probabilistic assessment of bearing pads, fragility curves are plotted to quantify the probability of shear failure of all eight bearing pad configurations due to five different wave time histories considered. Engineering demand parameters (EDPs) are taken as the maximum shear displacements from non-linear time history response for each bearing pad. The intensity measure for the development of fragility curves is taken as wave period (secs) to determine the probability of exceedance of shear displacement for each specific value of wave period. Each method is explained in detail in upcoming sections as follows:

3.1 Physics-based model (PBM) - AASHTO coastal guide (2023)

The hydrodynamic forces and moments depend upon the girder height, entrapped air, and wave parameters like wave height, wavelength, and wave period. Equations for forces and moments were first presented by (Morison et al. 1950) for vertical piles which are still being used for the force's calculation for vertical piles. Parameterized equations for bridge superstructure were developed by (Kaplan 1992) for an offshore platform deck that extended Morison's equations. These equations were valid for only thin horizontal structures and did not accurately represent bridge deck slabs having finite

thickness. Physics-based model equations developed by (Shepherd 2008) extended the Kaplan model to include the finite thickness of the deck impacting the overall deck mass for forces calculation. For this study, physics-based model (PBM) equations are used to calculate hydrodynamic forces in both horizontal and vertical direction. The American Association of State Highway and Transportation Officials (AASHTO) Coastal Guide (2023) has adopted these PBM equations and proposed three design equations for load application. One of the cases focuses on the overhang length of the bridge, which was not considered in this study. In Design Case I, the following forces were quantified and applied to the bridge: Associated Horizontal Quasi-Static Wave Force (FH-AV), Maximum Quasi-Static Vertical Force (FV-MAX), Vertical Slamming Forces (FS), and Associated Moment about the Trailing Edge due to the Quasi-Static and Slamming Forces (MT-AV). These forces were determined using equations provided in the AASHTO Coastal Guide. Similarly, for Design Case II, the forces applied included Maximum Horizontal Wave Force (FH-MAX), Associated Quasi-Static Vertical Force (FV-AH), Associated Vertical Slamming Force (FS), and Associated Moment about the Trailing Edge (MT-AH). Overall, the application of these hydrodynamic loads and equations from the AASHTO Coastal Guide (AASHTO 2023) ensures a comprehensive assessment of wave forces on the bridge structure, incorporating both conservative estimations and rigorous analytical techniques.

3.2 Wave time histories – linear wave theory

Coastal waves in actuality represent chaotic undulations which are often cumbersome to physically model. As such, the simplified yet effective "linear wave theory" presented by (Airy 1845) is presented and used in this study. According to this theory, waves are represented as linear sinusoidal waves while ignoring the Coriolis effect. Governing equations of motion are developed using lateral boundary condition, bottom boundary condition, kinematic free surface, and dynamic free surface boundary condition. These governing equations are differentiated spatially to obtain wave-particle displacements and accelerations for specific time domains. The wave acceleration time histories in this research study are based on the governing equation solution as follows:

$$\phi(x,z,t) = \frac{a.g}{\sigma} \cdot \frac{\cosh k(d+2)}{\cosh(kd)} \cdot \sin(kx - \sigma t) \tag{1}$$

$$ax = \frac{\partial \phi}{\partial x} = \frac{2\pi^2 H}{T^2} \cdot \left[\frac{\cosh k(d+z)}{\sinh(kd)}\right] .\sinh(kx - \sigma t) \tag{2}$$

where H is the wave height, T is the wave period in secs, d is the still water depth, z is the water surface elevation, x is the spatial distance, t is the time domain and σ is the wavelength.

Monte Carlo simulation is a computational technique that utilizes random sampling to approximate mathematical functions or analyze complex systems (Harrison 2010). Monte Carlo simulations have been utilized in this study to generate wave time histories, allowing for the incorporation of random values for wave height and period, which are crucial factors influencing wave time histories. Monte Carlo simulation had also been used previously by (Balomenos and Padgett 2018) to estimate the uncertain structural

capacities under the wave loading impact. In this research study, wave periods and wave heights were adopted from the ADCIRC model predictions by (Qu et al. 2021). Hurricane Sandy and predicted ADCIRC models had wave periods in the range of 6 secs to 18 secs and wave heights from 40 in. to 295 in. Random values of wave periods and heights are incorporated into governing equations outlined by (Dean and Dalrymple 1991) and originally developed by (Airy 1845) to generate one hundred acceleration time histories. Wave energy density was calculated as the criteria for further narrowing the wave histories which is referenced by (Goda 2010) with the combination of kinetic and potential energy as follows:

$$Ek = \int_0^L \int_{-d}^0 \frac{1}{2} \cdot \rho dxdz\left(u^2 + w^2\right) \tag{3}$$

$$Ep = \int_0^L \rho g.(d+\eta) \cdot \left(\frac{d+\eta}{2}\right) dx - \rho g L d\left(\frac{d}{2}\right) \tag{4}$$

$$E = Ek + Ep = \frac{1}{8} \cdot \rho \cdot g \cdot H^2 \tag{5}$$

where E is the energy density per unit area (J/in^2), p is the saline water density that is taken as 0.03 lb/in^3, g is the gravitational acceleration and H is the wave height which here is taken as significant wave height in inches. Twenty-five wave time histories were chosen as they almost represented the random wave parameters for wave periods of 8 secs to 11 secs. In Fig. 3, it can be noticed that five significant bands are observed with the first from 6 to 8 secs, the second from 8 to 12 secs, the third from 12 to 14 secs, the fourth from 14 to 16 secs and fifth from 16 to 18 secs. To make the analysis computationally efficient, it was decided to choose the maximum wave energy density from each of these five distinct bands. Based on the maximum energy impacted for each group, five wave time histories are chosen that are shown in Table 1, providing insight into the wave characteristics considered in the analysis.

It can be noted that time history TH-4 has the highest imparted energy per one wavelength. To investigate this, spatial temporal plots of five chosen time histories are presented in Fig. 4a-e.

These plots are oriented in a way that waves travel from one end of the spatial domain to another end in specific time. It can be observed that TH-4 with maximum frequency and wave height is approaching the acceleration of approximately 120 in/sec^2 whereas TH-5 with the lowest frequency and wave height approaches acceleration of only 20 in/sec^2.

3.3 Finite element analysis of bearing pads

Numerical analysis is performed in finite element analysis software Abaqus v6.11 (Abaqus, 2011) to capture the response of bearing pads subjected to cyclic loadings. Rezende et al. (2020) modeled bridge bearing pads using hyperelastic models like Neo-Hookean and Yeoh models that represented the response of bearing pads. Several other potential forms of strain energy potential are available including the Ogden model, but Neo-Hookean is the simplest model to simulate the response of elastomers in the

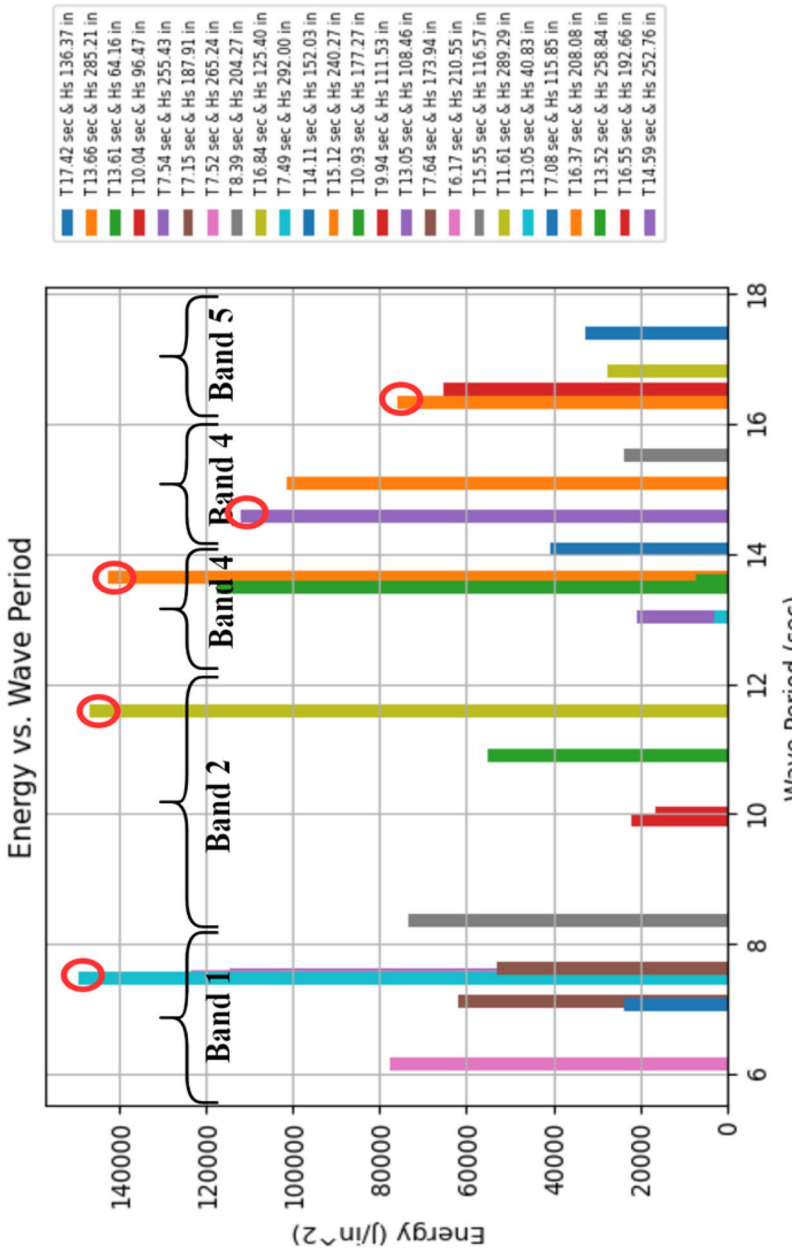

Fig. 3 Wave energy density in J/in^2: five distinct bands for 25 wave time histories resulted from Monte Carlo simulations

Table 1 Wave time histories

Time History	Wave Period (sec)	Wave Height (inches)	Wave energy (J/in^2)
TH-1	13.66	285.21	141,000
TH-2	11.61	289.29	142,000
TH-3	15.12	240.27	100,000
TH-4	7.49	292.00	**144,000**
TH-5	16.37	208.08	75,000

absence of accurate material data. The theoretical relevance of the Neo-Hookean potential lies in its mathematical analogy to the behavior of an ideal gas, particularly about the Helmholtz free energy of a molecular network with a Gaussian chain-length distribution (Treloar 1975). Neo-Hookean hyperelastic model parameters based on the general form of strain energy potential equations were chosen as follows. Due to incompressible material property, the second term in the below equation will be zero and merely will be dependent on the first term in which Cij is the factor dependent on the shear and elastic modulus of material whereas I1 and I2 are invariants of the polynomial equation.

$$U = \sum_{i+j=1}^{N} Cij\left(\overline{I1}-3\right)^{i} \cdot \left(\overline{I2}-3\right)^{j} + \sum_{i=1}^{N} \frac{1}{Di}(Jele-1)^{2i} \tag{6}$$

For numerical modeling purposes, four of the bearing pads BP1, BP2, BP3, and BP4 were chosen due to the brevity of the analysis. Linear elastic material was chosen for the abutment and piles to make the analysis computationally efficient. Non-linearity is induced in the analysis using the non-linear material hyperelastic models for the elastomeric pad. The penalty friction model was chosen for contact properties between the bearing pad and abutment concrete to represent the elastic-plastic behavior instead of the sticking friction for the elastic regime and slipping friction for the plastic regime. This is done to achieve the one-side bonded bearing pad which was also chosen for the analytical model. An eight-noded hybrid reduced integration hourglass brick element was chosen in which reduced integration interpolates the displacements on a single point. Hybrid (mixed) elements are chosen due to the incompressible behavior of hyperelastic material. Mesh sensitivity analysis was performed for bearing pad BP1 to choose the appropriate mesh size and that resulted in the mesh global size of "0.8" for bearing pad. For the cyclic loading response, TH-4, which had the greatest wave energy, was defined using the amplitude module. Acceleration time history was applied to structure as an acceleration boundary condition, which was used in the dynamic implicit analysis. The dynamic implicit analysis uses the equilibrium equations through the iterative process to calculate the bearing pad response parameters like displacements, strains, and stresses.

3.4 Fragility functions

Fragility functions quantify the probability of failure such that demand does not exceed capacity for an intensity measure. Fragility function can be defined in terms of the conditional probability as follows:

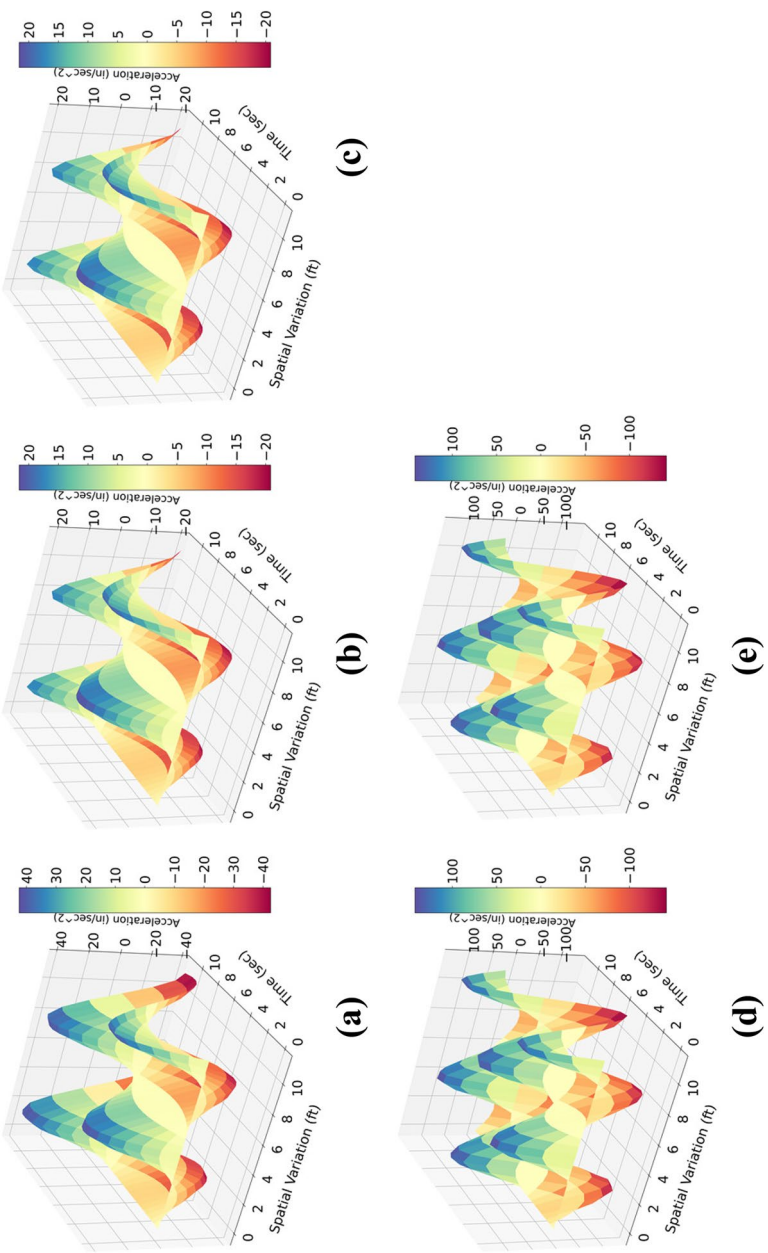

Fig. 4 Spatial-temporal acceleration time histories **a** TH1 **b** TH2 **c** TH3 **d** TH4 **e** TH5

$$P(D|IM = x) = \phi \cdot \frac{\left(\ln\left(\frac{x}{\theta}\right)\right)}{\beta}; \tag{7}$$

where β= Dispersion coefficient, θ= Engineering demand parameters (EDPs) are maximum shear displacements corresponding to each bearing pad, D = Damage State, x = IM, intensity measure which is wave period (secs) in this case, ϕ=Cumulative probability distribution of random variables which in this case are wave period and shear displacements. Damage states and Engineering demand parameters (EDPs) are shown in Table 2.

4 Modeling & analysis

4.1 Bearing pads modeling

Bearing pads play a critical role in transferring loads between different structural elements while accommodating movements caused by thermal expansion, creep, and live loads. They are typically made from elastomeric materials like neoprene or natural rubber, which exhibit nonlinear behavior such as stress softening and strain hardening. Key considerations in bearing pad modeling include implementing appropriate material models, defining contact interfaces between the pads and adjacent elements, and accounting for geometric nonlinearities under severe loading conditions. To incorporate the geometric non-linearity and appropriate material models bearing pads are represented in this study as non-linear links, where their behavior is akin to a system of springs accounting for axial, shear, and bending deformations as shown in Fig. 5a. Bearing pads had also previously been modeled as non-linear links by (Peng et al. 2023) for the numerical modeling of bridge expansion joint systems. In this representation, shear forces are typically considered at a distance "dj" from each joint, allowing for a more accurate depiction of the pad's response to loading. The stiffness of these springs is computed based on the material properties of the pad and its geometric characteristics, ensuring a realistic simulation of its behavior under various conditions. Moreover, it is important to note that the axial forces and displacements primarily affect the depth axis (H) (1) of the pad, while shear forces influence its length (L) (2) and width (W) (3) axes, providing insight into how different loading scenarios impact the pad's structural integrity and performance. This approach facilitates a comprehensive understanding of the complex interaction between bearing pads and their supporting elements within the overall structural system.

Table 2 Damage states (DS1 to DS5) & Engineering demand parameters (EDPs)

Damage State (D)	Wave Period (sec)	Bearing Pad Configurations	Engineering Demand Parameters (EDPs, in)
DS 1	7.49	BP 1	1.90
DS 2	11.61	BP 2	0.65
DS 3	13.66	BP 3	1.96
DS 4	15.12	BP 4	0.69
DS 5	16.37	BP 5	1.70
		BP 6	2.88
		BP 7	2.71
		BP 8	3.22

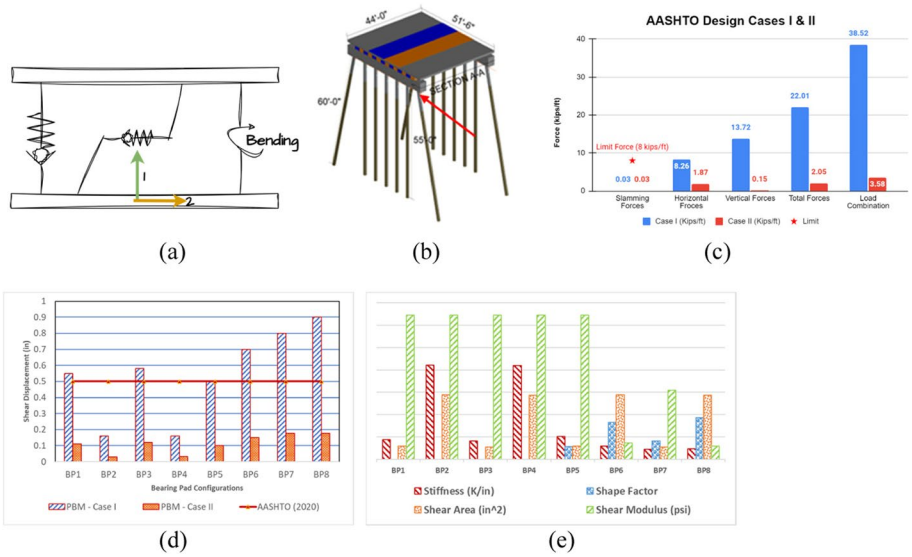

Fig. 5 **a** Bearing pad modeling as non-linear link. **b** Typical East Coast bridge 3D model. **c** Comparison of AASHTO design forces – design case I & case II. **d** Shear deformations due to physics-based models (PBMs) design case I & case II. **e** Stiffness variation as a function of shape factor, shear moduli & shear area

Table 3 Bearing geometry & stiffnesses

Bearing Pad	Bearing Size	Gpad (psi)	Shape Factor (S)	Shear Stiffness (K/in)
SAP 2000 Analysis Reference Manual, 2014				
BP1	24″ × 5″ × 0.75″	129	-	17.6
BP2	24″ × 24″ × 0.75″		-	84.4
BP3	12″ Diameter		-	16.6
BP4	27″ Diameter		-	83.3
Roeder et al. 1987 **&** Yazdani et al. 2000				
Reinforced (4 layers)	**Bearing Size**	**Gpad (psi)**	**Shape Factor (S)**	**Shear Stiffness (K/in)**
BP5	24″ × 5″ × 0.75″	129	11.4	20.63
BP6	24″ × 24″ × 0.75″	15	33.3	11.8
BP7	12″ Diameter	62	16.6	9.29
BP8	27″ Diameter	12	37.5	9.33

For the sake of the parametric study, different bearing pad configurations are chosen based on varied sizes and analytical stiffness models from (Yazdani et al. 2000; Roeder et al. 1987) & CSI Bridge analysis reference manual (CSI Bridge,2014). Eight bearing pad configurations with plain and reinforced bearing pads with rectangular and circular geometries are shown in Table 3. Four of them are taken as plain elastomeric pads without any reinforcement and are well represented by basic mechanical models, however for reinforced pads two models are used in which square pads are represented (Yazdani et al. 2000) and circular reinforced pads are represented by (Roeder et al. 1987). A shear modulus of 129 psi and an elasticity modulus of 375 psi has been used from mechanical models presented in AASHTO LRFD (AASHTO 2020). However, for other models, the shear modulus is a function of the rubber

hardness, elasticity modulus, and shape factor as stated, where the shape factor is the function of each elastomer layer dimensions as follows:

$$Epad = 3Gpad \cdot \left(1 + kS^2\right) \tag{8}$$

$$S = \frac{L \cdot W}{2h(L+W)} \text{ (Yazdani et al.(2000) Rectangular pads)} \tag{9}$$

$$S = \frac{D}{4h} \text{ (Roeder et al.(1987) Circular pads)} \tag{10}$$

Bearing pads of 50 Durometer hardness with a "k" value of 0.75 were chosen to calculate the pad elasticity modulus used to calculate the shear modulus of rigidity.

4.2 Non-linear modal time history analysis--fast non-linear analysis

In addressing computational challenges, the Fast Non-Linear Analysis (FNA) method, pioneered by (Ibrahimbegovic and Wilson 1989; Wilson 1993), offers a promising solution. FNA proves particularly beneficial when the overarching structure retains elasticity while individual components demonstrate nonlinear behavior. In modal time history analysis, the dynamic response of a structure is computed by considering the modal decomposition of the system's response. The modal decomposition involves representing the structural response as a linear combination of the mode shapes of the structure. These mode shapes are the natural vibration modes of the structure obtained from modal analysis. The equilibrium equation can be written as follows:

$$M\ddot{u}(t) + C\dot{u} + Ku(t) = r(t) - [rN(t) - KNu(t)] \tag{11}$$

Where $K = KL + KN$, r is the vector of applied loads, and rN is the vector of forces from the non-linear degree of freedom of link/support. KL is the stiffness matrix of all linear elements other than links/supports whereas KN is the stiffness matrix for nonlinear degrees of freedom of links/supports.

The Bouc-Wen model, initially proposed by (Bouc 1967) and later extended by Wen in 1976, is a mathematical model used to describe hysteresis, a phenomenon commonly observed in physical systems where the response of a system depends not only on its current state but also on its history. Nonlinearity in links is introduced through the implementation of Wen's plasticity model (Wen 1976), which associates post-yielding stiffness ratios with plastic deformation across each degree of freedom. The Bouc-Wen model indeed stands out as one of the most popular and versatile models for hysteresis. It falls under the category of endochronic models, as noted by (Valanis 1971). Its extensive application has led to the designation of a whole class of hysteresis models bearing its name, highlighting its significance and widespread adoption in various fields of science and engineering. This model facilitates decoupled nonlinear responses, allowing for a more accurate representation of structural behavior under varying loading conditions. The plasticity model formulation, as follows, governs the deformation characteristics of the links, and contributes to the simulation of a realistic structural response.

$$\boldsymbol{f} = ratio.k.d + (1 - ratio).yield.z \tag{12}$$

Whereas in the above equation k is the stiffness, yield is the yield strength and ratio are the ratio of post yield stiffness to elastic stiffness (k) and z is the internal hysteresis model.

5 Case study bridge

A multi-stringer prestressed concrete T beam bridge, spanning 44 ft and supported by bent abutments is chosen for analysis. The abutments feature fourteen 3 ft wide concrete box girders and seven piles each, with a diameter of 1.5 ft. Notably, the exterior piles are inclined at angles of 75.96° and 14.04°, while interior piles measure 55 ft, and exterior piles extend to 60 ft. A 3D model of the bridge is shown in Fig. 5b which is modeled in CSI Bridge v22.2.0 (CSI Bridge 2014). The bridge, originally designed as a 44 ft single-span structure, features a concrete girder section with beam dimensions and web thickness adjusted to a height of 1.417 ft and width of 3 ft. While the bridge initially comprised precast beam sections, they were modeled as reinforced concrete beams with a concrete compressive strength of 5,250 psi to accurately capture the response of bearing pads to wave loads. The start and end abutments were designated as bents, supported by seven 18-inch diameter columns each.

6 Results and discussion

6.1 Physics-based model (PBM)

Bridges vulnerable to wave or surge forces are designed for the strength limit using the load combinations presented in the AASHTO Coastal Guide (AASHTO 2023) as presented in the below equation. Vertical and horizontal forces are computed for both design cases I & II in which maximum vertical forces plus slamming force was applied for Case I and maximum horizontal forces were applied for Case II. These forces are applied as line loading along the bent beam length for both cases and distributed moments are applied along the bent beam length.

$$\gamma_p DC + \gamma_p DD + \gamma_p DW + \gamma_p EL + \gamma_{wave} WA \tag{13}$$

Other than the slamming forces, quasi-static vertical and horizontal forces exceeded the smallest limit force of 8 kips/ft AASHTO Coastal Guide (AASHTO 2023). This can also be observed that overall vertical forces were more dominant in both Design Case I and Case II as shown in Fig. 5c.

6.1.1 Shear displacements due to quasi-static forces – PBM

Horizontal forces are applied as lateral equivalent forces to bridge the trailing edge to capture the shear response of bearing pads. Shear deformations for plain elastomeric pads depend on the shear area and rigidity of the bearing pad, and shear deformations for reinforced pads depend on shape factor and shear area. Shear deformations for associated horizontal quasi-static forces and maximum horizontal quasi-static forces are shown in Fig. 5d.

For Case I, it can be observed that the largest shear displacement of 0.8 in for reinforced pads BP7 (circular 12” Dia) and 0.9 in for BP8 (circular 27” Dia) exceeded the AASHTO limit for shear deformation i.e., 0.5 in. Greater shear deformation for circular reinforced pads of larger size is attributed to the more shear area to deform. Additionally,

reinforced circular pads are deformed 60% to 80% more than of square and rectangular reinforced pads and this can be attributed to the fact that shape factors for circular pads are greater than that of square & rectangular pads and hence resulted in increased stiffness of square & rectangular pads. Overall, reinforced pads are having more shear displacements as compared to the PEPs because reinforced pads are not only a function of the shear deformable area but also dependent on the shape factor that resulted in the varied shear moduli of reinforced pads. Figure 5e shows the variation of stiffness as a function of shape factor and shear area. Similarly, for Case II, the behavior is the same as in Case I with the difference that deformations are ¼ times of Case I. This is due to the reason that vertical forces for Case II are way less than Case I due to exponential decay of associated vertical forces. This exponential decay is further attributed to the physics-based models developed in such a way as to have a restrained response of substructure in the horizontal direction for Case II.

6.2 Shear displacements due to cyclic wave loadings

Two primary scenarios are investigated for all bearing pad configurations due to cyclic wave loadings: scenario 1 explores different time histories for the same link tag, while scenario 2 examines different link tags for the same time history.

6.2.1 Different wave time histories for the same bearing link

Five load cases are established using non-linear modal time history analysis, with acceleration applied along the Global Y axis, corresponding to the local 1 axis of bearing pads, due to the direction of water flow along the Y axis in the case study bridge. Scenario 1 is further subdivided into two cases: One is the response of plain elastomeric pads (PEPs) with two rectangular and two circular geometries for shear resistance. Second is the response of reinforced pads with four embedded layers due to lateral forces.

Bearing pad BP1 was specifically chosen to match the size used in the bridge structure under research study. While the acceleration is applied in the Global Y direction, the focus here lies on examining the response in the local 1 axis of each bearing pad. It is worth noting that the bearing pads are assumed to be bonded on the bottom face, showing that they are not bonded or reinforced to the girders at the top. The responses are displayed for eight bearing pads for each wave time history. Notably, for TH-4, corresponding to the time history with the highest wave energy, the hysteresis loops appear wider compared to other responses. Wider energy loops depict the greater energy dissipation showing that for each bearing pad configuration, TH-4 resulted in the largest area enclosed by the loop. This observation suggests that shear forces induce higher energy dissipation and the highest shear displacement of 1.96 inches. This is also supported by (Xiang and Li 2016) experimental tests for single side bonded pads which resulted in maximum displacement of 2 inches. However, it can also be observed that for BP3 i.e., the circular pad having an equivalent cross-sectional area of BP1, shear displacements increased the experimental test results hence imposing a more detailed response using a numerical model. In general, all PEPs and reinforced pads exceed the limit shear deformation of 0.5 inches for TH-4 (AASHTO 2020). Interestingly cyclic loading resulted in increased deformation for each loading cycle, and it can also be seen that bearing pads

BP1 and BP3 have less stiffness as compared to the BP2 and BP4 which can also be depicted from the slope of the hysteresis loop and as shown in the Fig. 6a-d.

Steel-reinforced elastomeric bearings are considered separately from other types of elastomeric bearings due to their superior strength and performance in real-world applications, as highlighted by (Roeder et al. 1987). Figure 7e-h illustrates the hysteresis response for shear displacement in the local 1-axis direction. For reinforced pads, cyclic loading resulted in larger shear displacements as compared to the equivalent quasi-static forces implicating the strain energy loss over the loading cycles. In addition, reinforced pads also have more shear displacements than plain elastomeric pads (PEPs). BP 8 has the largest shear displacement of 3.2 inches for TH-4, which is higher than the test data, and a shear deformation limit of 0.5 inches. This is due to the influence of the highest shape factor of "37.5" as proposed by (Roeder et al. 1987). These observations are supported by experimental evidence from quasi-static tests conducted to investigate the cyclic behaviors of top-side bonded bridge elastomeric bearings under lateral loads.

6.2.2 Different bearing links for same wave time history (TH-4)

In this scenario, the responses of all bearing pads are meticulously scrutinized for TH-4, characterized by notably higher wave energy and the utmost wave height among the considered cases. Figure 7i illustrates the responses of all bearings for TH-4. Notably, reinforced bearing pads BP6 and BP8 resulted in more deformation over the same number of loading cycles as compared to the experimental data, BP 5 & BP 7. All these four pads are reinforced but rectangular pads behaved well as compared to the plain elastomeric pads resulting in less energy loss over cyclic wave loadings. Unlike seismic demands, where energy dissipation positively contributes to structural response, storm surge forces present a contrasting scenario. Here, energy dissipation in bearing connections signifies failure or near-failure due to the lift-off force exerted by the wave forces. Therefore, in the presence of the lift-off force, energy dissipation results in the failure of the bearing connection. This comparison also identifies that none of the bearing pads for TH4 had shear displacements within the recommended AASHTO limits of 0.5 inches due to the reduced stiffness over the number of cycles during wave loadings.

6.3 Shear displacements due to cyclic wave loadings –finite element model

To capture the detailed response of the circular and rectangular bearing pads, the hysteresis response of bearing pads is plotted for BP 1 to BP 4 using a numerical model. Experimental data from uniaxial, biaxial, and planar testing of hyperelastic material at temperature of 20 °C is taken from (Duncan et al. 1999) as shown in Fig. 7a-c. The reason for choosing the experimental data is to optimize the material models to truly represent the response of hyper elastic elastomeric rubber pad. Four material models were evaluated against the experimental test data for stability in each planar, uniaxial, and biaxial response. It is worth noting that the material model used for the analytical model was not used due to the reason that Xiang Li tested the pad for shear deformation alone which is insufficient for choosing the material model representing the hyperelastic material. Figure 7d shows the stress-strain relationship using Arruda Boyce, Marlow, Ogden, and Neo-Hookean models along with the test data for each uniaxial, biaxial, and planar test. The neo-Hookean model closely matched all three tests' data, hence verifying

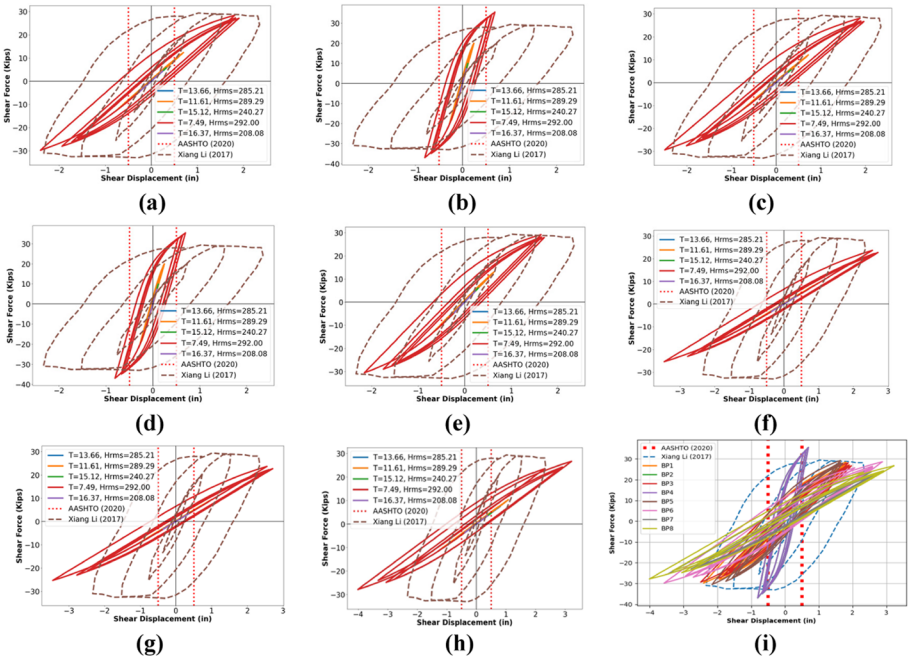

Fig. 6 Hysteresis response due to varying wave time histories for plain elastomeric pads (PEPs) **a** BP1 **b** BP2 **c** BP3 **d** BP4; for reinforced bearing pads **e** BP5 **f** BP6 **g** BP7 **h** BP8; hysteresis response for bearing pads BP1 to BP8 due to **i** time history TH-4

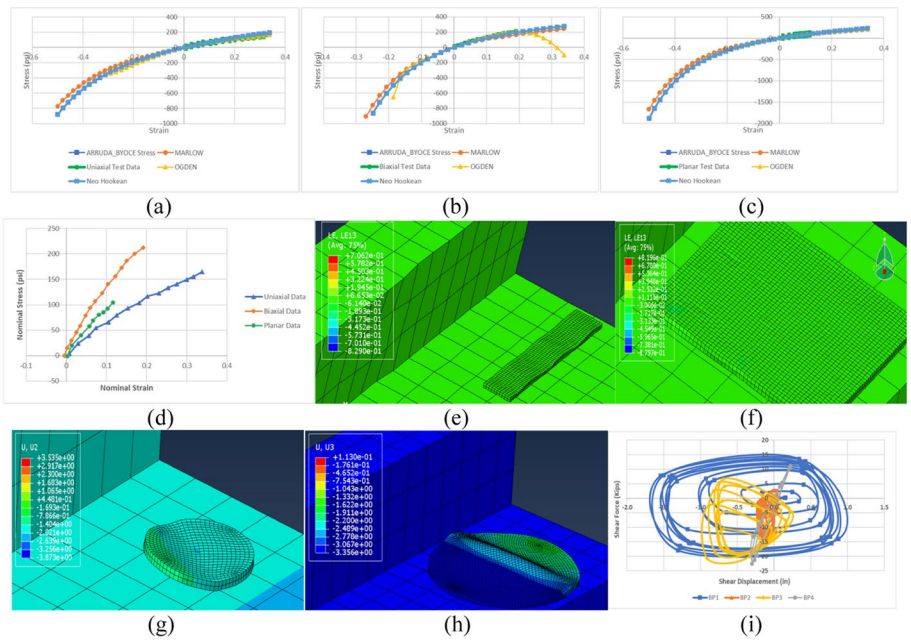

Fig. 7 Material models evaluation. **a** Biaxial test data. **b** Uniaxial test data. **c** Planar test data. **d** Experimental data -hyper elastic material test data at 20 °C (Duncan et al. 1999); deformed elastomeric rubber pad for Neo-Hookean material model for time history TH-4 **e** BP1 **f** BP2 **g** BP3 **h** BP4; **i** hysteresis response of bearing pads for time history TH-4

the reason being this model used widely to model hyperelastic material using the neo-Hookean material model. Although for uniaxial and planar tests, other models are also stable and match test data, they are not stable for the biaxial test. This instability could be due to the more complex stress state introduced by the biaxial test, which some models may not accurately capture. Additionally, the different assumptions and mathematical formulations underlying these models might not hold under biaxial loading conditions.

Figure 7e-h shows the deformed shapes of unreinforced bearing pads. This was assumed in the study that there is no shear resistance due to friction and no axial loads were considered. These deformed shapes represent the incompressibility of the hyperelastic material. It can be shown that despite the hard contact property representing the bonded bottom face, bearing pads will be deformed in such a way that wave loadings are inducing significant shear deformations and this can be attributed to having low assumed friction between the bearing pad and concrete surface. Additionally, the increased fragility of the smaller cross sections of both circular and rectangular pads can be depicted from the deformed shapes that is also supported by the hysteresis responses from analytical models discussed above. Figure 7i shows the hysteresis response of four bearing pads using the Neo-Hookean model which depicts the maximum hysteresis loss of BP1 and the least hysteresis loss of BP4. This shows the resilience of bearing pads with larger cross-sections. It can also be depicted that the different behavior of circular pads from square pads is due to its significant displacement along the z-axis i.e., along the depth of the pad. The upward movement of bearing pad corners could be attributed to the uplift of the deck hence reducing the dead weight of girders on bearing pads leaving pads flexible to deform. Larger bearing pads have less stiffness and more displacements for the same number of cycles than smaller pads, and it resembles the hysteresis response from analytical models. Note that hysteresis loops using numerical models do not resemble the backbone curve from Plastic Wen model because in numerical models, these elastomeric pads are modeled as hyper elastic material. The slope and plump degree of force-displacement hysteresis curves are correlative with the stiffness and energy dissipation of the bearing pad, respectively as also presented by (Mandani et al. 2023).

6.4 Comparative analysis

Figure 8 compares shear displacements for different bearing pad configurations (BP1 to BP8) using various analytical methods: PBM - Case I, PBM - Case II, a Numerical Model, and Airy's Theory (TH4). Airy's Theory (TH4) consistently predicts the highest shear displacements, ranging from approximately 0.7 inches for BP2 to 3.2 inches for BP6, showing a conservative approach that overestimates displacements to ensure safety. The Physics-Based Model (PBM) in both Case I and Case II scenarios shows moderate shear displacements. For instance, in BP1, PBM - Case I predicts about 0.51 inches while Case II predicts around 0.2 inches. The Numerical Model tends to predict the highest value of about 1.6 inches for BP1 and the lowest value of about 0.3 inches for BP2. This comparison highlights that while AASHTO LRFD (AASHTO 2020) and (Xiang and Li 2016) provide practical, standardized benchmarks for shear displacement, these limits alone may not be sufficient to predict shear failure accurately. The models have exceeded these standardized limits, suggesting that more detailed and specific analyses are necessary to

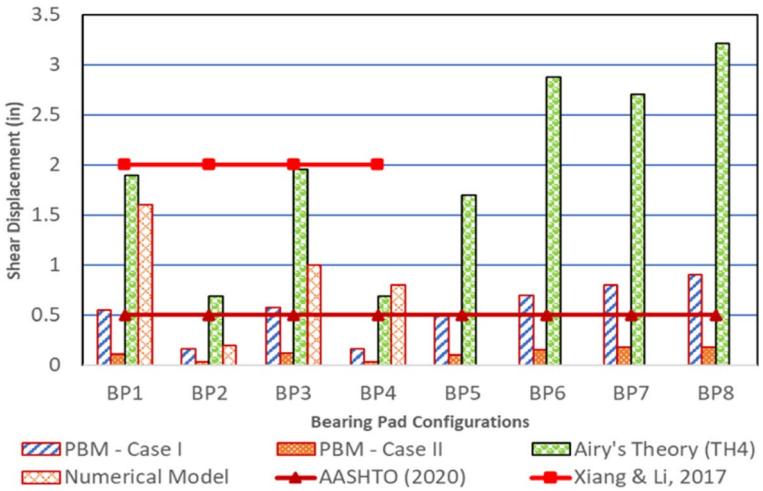

Fig. 8 Comparative analysis of different modeling techniques for shear displacements due to hurricane-induced wave loadings

ensure the safety and reliability of bearing pad designs for bridges susceptible to hurricane-induced wave loadings.

This analysis reveals the limitations of AASHTO LRFD (2020), as the study's models exceeded these standardized limits, suggesting that more detailed and specific analyses are necessary for accurately predicting shear failure when analyzing hurricane-induced wave loadings. This underscores the importance of selecting appropriate materials and designs that account for both shear area and shape factors. Moreover, the analysis of hysteresis loops reveals significant energy dissipation, particularly in scenarios with lower wave periods and larger wave heights, indicating the need to enhance the damping characteristics of bearing pads. By incorporating these insights into design and evaluation processes, engineers and researchers can significantly improve the resilience and reliability of bridge structures in coastal regions, ensuring they can withstand extreme coastal hazards.

7 Fragility curves

Fragility functions for all bearing pads subjected to five-time histories (TH) are generated as shown in Fig. 9. For this research study, the engineering demand parameters (EDPs) used are shear displacements of the bearing pad, IM is wave period (sec) and damage states DS1 to DS 5 are shear displacements corresponding to five wave time histories. The time history, TH-4, has maximum wave height and lowest wave period, which can also be evident from the maximum hysteresis loss for TH-4-time history. Similarly, the least fragilities of all bearing pads are for TH-5-time history i.e., with highest wave period and least wave height. The overall trend of fragilities of bearing pads is the same across all time histories in terms of the bearing pad BP8 having the highest fragility and BP4 having the lowest fragility. For the time history TH-4, the probabilities that the shear displacements of various bearing pads exceed the damage state limit DS1 are as follows: bearing pad BP8 has a 98% probability, BP7 has an 89% probability, BP6 has a 92% probability, BP5 has a 76% probability, both BP4, and BP2 have a 58%

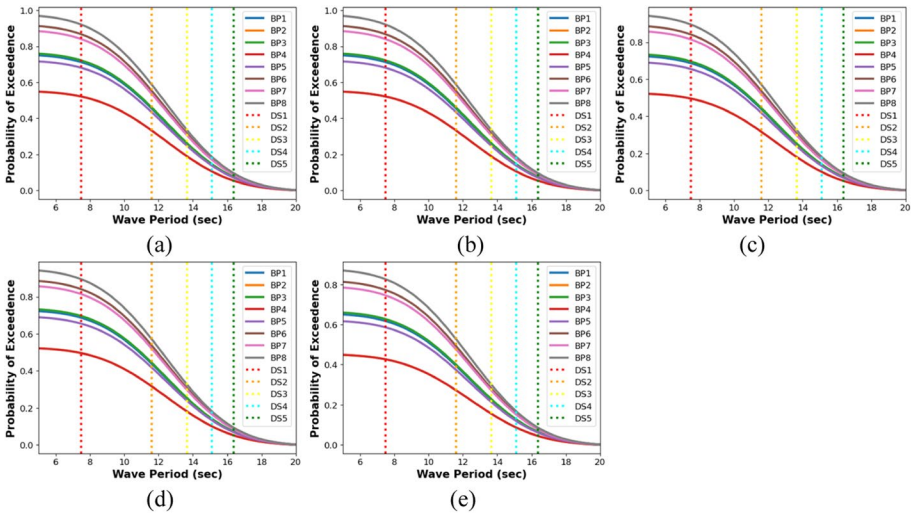

Fig. 9 Fragility functions for bearing pads BP1 to BP8 for time histories **a** TH4 **b** TH2 **c** TH1 **d** TH3 **e** TH5

Table 4 Probabilities of failure of bearing pads BP1 to BP 8 - damage state DS-1

Bearing Pad Configuration	Probability of Failure (TH-4)	Probability of Failure (TH-5)
BP 1	0.78	0.64
BP 2	0.58	0.42
BP 3	0.78	0.64
BP 4	0.58	0.42
BP 5	0.76	0.61
BP 6	0.92	0.81
BP 7	0.89	0.78
BP 8	0.96	0.84

probability, and both BP3 and BP1 have a 78% probability. It is worth noting that with an increasing wave period, the probability of exceedance for each bearing pad is also decreasing. This can be observed from the fact that for damage state DS 5, fragilities of all bearing pads range from 10 to 15% with the least amount of dispersion. Probabilities of failure for time histories TH-4 & TH-5 corresponding to damage state DS-1 are presented in Table 4.

8 Summary & conclusion

Several past studies have analyzed for studying the response of bridge connections, particularly bearings, due to hurricane-induced wave loadings; however, there is a knowledge gap in capturing the non-linear dynamic response of connections with different configurations when subjected to cyclic wave loadings such that the importance of hysteresis response and energy dissipation are captured in response. To emphasize this, the quasi-static response of bearing pads using physics-based models (PBMs) from AASHTO Coastal Guide (2023) is compared with a non-linear dynamic response. This study models bearing pads as nonlinear links to analyze quasi-static wave loadings and wave time history effects using fast nonlinear analysis (FNA). The stiffness of these

non-linear links is computed based on the material properties of the pad and its geometric characteristics, ensuring a realistic simulation of its behavior under various conditions. Moreover, it is important to note that the axial forces and displacements primarily affected the depth axis (H) (1) of the pad, while shear forces influenced its length (L) (2) and width (W) (3) axes, provided insight into how different loading scenarios impact the pad's structural integrity and performance. This approach facilitated a comprehensive understanding of the complex interaction between bearing pads and their supporting elements within the overall structural system. FNA is particularly beneficial when the overarching structure retains elasticity while individual components demonstrate non-linear behavior.

For PBMs, it was observed that the largest shear displacement reinforced pads BP7 and BP8 exceeded the AASHTO limit for shear deformation. Greater shear deformation for the circular reinforced pad of larger size i.e. BP8 as compared to the circular reinforced pad of smaller size i.e. BP7 was attributed to the more shear area to deform. Additionally, reinforced circular pads deformed more than that of square and rectangular reinforced pads and this can be attributed to the fact that shape factors for circular pads are greater than that of square & rectangular pads and hence resulted in increased stiffness of square & rectangular pads. Overall, reinforced pads were having more shear displacements as compared to the PEPs because reinforced pads are not only function of the shear deformable area but also dependent on the shape factor that resulted in the varied shear moduli of reinforced pads. For non-linear time history analysis (NLTHA), hysteresis loops highlighted significant energy dissipation in scenarios with lower wave periods and highest wave heights, particularly in time history TH-4. These loops identified that none of the bearing pads for TH-4 had shear displacements within the recommended AASHTO limits due to the reduced stiffness over several cycles during wave loadings. For the numerical model, the Neo-Hookean hyperelastic model best represented elastomeric pad responses, outperforming other material models in reflecting experimental shear stress-strain relationships. The hysteresis response of four bearing pads using the Neo-Hookean model depicted the maximum hysteresis loss of BP1 and the least hysteresis loss of BP4. This shows the resilience of bearing pads with larger cross-sections. The different behavior of circular pads from square pads was due to its significant displacement along the z-axis i.e., along the depth of the pad. The upward movement of bearing pad corners was attributed to the uplift of the deck hence reducing the dead weight of girders on bearing pads leaving pads flexible to deform. Larger bearing pads had less stiffness and more displacements for the same number of cycles than smaller pads, and it resembled the hysteresis response from analytical models. The shape of hysteresis loops using numerical models did not resemble the backbone curve from the Plastic Wen model because, in numerical models, these elastomeric pads were modeled as hyperelastic material.

For probabilistic assessment of bearing pads failure, uncertainties were incorporated by using Monte Carlo simulations for random variables i.e. wave period and shear displacements. The overall trend of fragility of bearing pads was the same across all time histories in terms of the bearing pad BP8 i.e. circular reinforced pad with larger size having highest fragility and BP4 i.e. plain circular bearing pad having lowest fragility. For the time history TH-4, the probabilities that the shear displacements of various bearing pads

exceeded the damage state limit DS1 were more than other time histories. It is worth noting that with an increasing wave period, the probability of exceedance for each bearing pad was also decreasing without significant dispersion.

Elastomeric rubber pads are highly incompressible, and most often reinforced with steel plates to increase the axial ability but they are more vulnerable to shear deformations caused by hurricane-induced wave loadings. The detailed analysis of different bearing pad configurations and their hysteresis response to hydrodynamic forces provides practical guidance for selecting materials and design parameters that optimize performance and durability. Overall, this research contributes to the advancement of performance-based design methodologies, equipping engineers with the tools and knowledge necessary to mitigate the risks associated with extreme coastal hazards. Future studies could focus on the numerical modeling of reinforced pads as well to compare the response of PEPs and reinforced pads. Linear wave theory is used in this study, however non-linear wave theories can be implied as well to capture the structural response due to Coriolis forces. Other than PEPs and reinforced pads, other types like pot bearings can also be used to capture the hysteresis response and to extend this study further on other bearing types. Research can also be extended to find the practical solution for bearings that are not only sufficient for resisting larger axial loadings but also to resist induced shear deformations due to hurricane induced wave loadings. Experimental validation of the numerical findings in this paper through prototype testing in a wave tank could enhance the reliability and applicability of the results in real-world bridge engineering practices.

Acknowledgements
This work could not have been carried out without the help of undergraduate researcher Annabelle Dorsett and undergraduate researcher Adriana M. Mercado Cruz.

Authors' contributions
WI carried out the design, conception, and analyses throughout the manuscript. MH secured project funding and provided guidance on the methodology and results, and edited the paper for final submission.

Funding
This material is based upon work supported by the US Army Corps of Engineers, ERDC Contracting Office under Contract No. W912HZ-22-2-0015.

Availability of data and materials
The datasets used and/or analyzed during the current study are available from the corresponding author on reasonable request.

Declarations

Competing interests
The authors declare that they have no competing interests.

Received: 10 June 2024 Accepted: 4 August 2024
Published online: 11 October 2024

References

AASHTO (2020) LRFD bridge design specifications
AASHTO (2023) Guide specifications for bridges vulnerable to coastal storms
Abaqus G (2011) Abaqus 6.11. Dassault Systems Simulia Corporation, Providence, RI, USA
Airy GB (1845) On tides and waves, Encyclopedia Metropolitana. London: B. Fellowes, 5:241–396
ASCE (2016) Minimum design loads and associated criteria for buildings and other structures. ASCE 7-16. ASCE, Reston
ASCE (2022) Minimum Design Loads and Associated Criteria for Buildings and Other Structures. ASCE 7-22. Reston, VA: ASCE
ASCE (2021) www.infrastructurereportcard.org/bridges/, retrieved 8/8/2014

ASCE (2023) Supplement 2 for Minimum Design Loads and Associated Criteria for Buildings and Other Structures (ASCE/SEI 7-22)
Ataei N, Padgett JE (2013) Limit state capacities for global performance assessment of bridges exposed to hurricane surge and wave. Struct Saf 41:73–81. https://doi.org/10.1016/j.strusafe.2012.10.005
Ataei N, Stearns M, Padgett JE (2010) Response sensitivity for probabilistic damage assessment of coastal bridges under surge and wave loading. Transp Res Rec 2202(1):93–101
Attary N, Unnikrishnan VU, van de Lindt JW, Cox DT, Barbosa AR (2017) Performance-based tsunami engineering methodology for risk assessment of structures. Eng Struct 141:676–686. https://doi.org/10.1016/j.engstruct.2017.03.071
Attary N, Van De Lindt JW, Barbosa AR, Cox DT, Unnikrishnan VU (2019) Performance-based tsunami engineering for risk assessment of structures subjected to multi-hazards: tsunami following earthquake. J Earthq Eng 2019:1–20. https://doi.org/10.1080/13632469.2019.1616335
Balomenos GP, Padgett JE (2018) Fragility analysis of pile-supported wharves and piers exposed to storm surge and waves. J Waterw Port Coast Ocean Eng 144(2):04017046
Barbato M, Petrini F, Unnikrishnan VU, Ciampoli M (2013) Performance-based hurricane engineering (PBHE) framework. Struct Saf 45:24–35. https://doi.org/10.1016/j.strusafe.2013.07.002
Boin A, McConnell A (2007) Preparing for critical infrastructure breakdowns: the limits of crisis management and the need for resilience. J Conting Crisis Manag 15(1):50–59
Bouc R (1967) Forced vibrations of mechanical systems with hysteresis. In: Proc. of the fourth conference on nonlinear oscillations, Prague, 1967
Ciampoli M, Petrini F, Augusti G (2011) Performance-based wind engineering: towards a general procedure. Struct Saf 33(6):367–378. https://doi.org/10.1016/j.strusafe.2011.07.001
CSI Bridge (2014) CSI Bridge analysis reference manual. I: Berkeley (CA, USA): Computers and Structures INC
Cui W, Caracoglia L (2018) A unified framework for performance-based wind engineering of tall buildings in hurricane-prone regions based on lifetime intervention-cost estimation. Struct Saf 73:75–86
Dean RG, Dalrymple RA (1991) Water Wave Mechanics for Engineers and Scientists. Adv Ser Ocean Eng 2
Do TQ (2016) Fragility Approach for Performance-Based Design in Fluid Structure Interaction Problems, Part I: Wind and Wind Turbines, Part II: Waves and Elevated Coastal Structures. Colorado State University
Duncan BC, Maxwell AS, Crocker LE, Hunt RA (1999) Verification of hyper elastic test methods. NPL report. CMMT(A)226
FEMA (2011) Coastal construction manual vol.1. Principles and practices of planning, siting, designing, constructing, and maintaining residential buildings in coastal areas, 4th ed. FEMA P-55
FEMA (2021) American Society of Civil Engineers - flood resistant design and construction
Goda Y (2010) Reanalysis of regular and random breaking wave statistics. Coast Eng J 52(1):71–106
Guo A, Fang Q, Bai X, Li H (2015) Hydrodynamic experiment of the wave force acting on the superstructures of coastal bridges. J Bridg Eng 20(12):04015012
Harrison RL (2010) Introduction To Monte Carlo Simulation. AIP Conf Proc 1204:17–21. https://doi.org/10.1063/1.3295638
Hosseini SA (2022) Evaluation of shape factor effect on hysteresis behavior of elastomeric rubber bearings. Int J Adv Struct Eng 12:661–670
Huang B, Yang Z, Zhu B, Zhang J, Kang A, Pan L (2019) Vulnerability assessment of coastal bridge superstructure with box girder under solitary wave forces through experimental study. Ocean Eng 189:106337
Huang B, Liao L, Ren Q, Cui X, Zhang J, Zhu B (2022) Fragility analysis of the box-girder coastal bridge with different connections subjected to extreme random waves. Ocean Eng 245:110580
IBC (2018) International Building Code (IBC), The International Code Council (ICC). IL, USA
Ibrahimbegovic A, Wilson EL (1989) Simple numerical algorithms for the mode superposition analysis of linear structural systems with non-proportional damping. Comput Struct 33(2):523–531
Ingargiola JL, Jones CP, Quinn RC (2013) ASCE 24: improving the performance of buildings and structures in flood hazard areas. In: Advances in hurricane engineering: learning from our past. p 53–66
Iqbal W, Head MH, Gac M, Dorsett A, Albanese M (2023) Assessment of residential construction due to sea-level rise and saltwater intrusion. In: ASCE Inspire 2023. p 516–528
Kaplan P (1992) Wave impact forces on offshore structures: re-examination and new interpretations. In: Offshore technology conference (OTC-6814)
Krahl PA, Vidigal de Lima MC, Siqueira GH (2020) Simplified analytical nonlinear model for contact problem between precast concrete beams and elastomeric bearing pads. J Struct Eng 146(11):04020251
Lehrman JB, Higgins C, Cox D (2012) Performance of highway bridge girder anchorages under simulated hurricane wave induced loads. J Bridg Eng 17(2):259–271
Mandani AM, Hejazi F, Nikkhoo A (2023) Development of a hybrid rubber damper-restrainer (HRDR) system for structures under severe dynamic excitation. Structures 55:1354–1387
Moeini M, Memari AM (2023) Hurricane-induced failure mechanisms in low-rise residential buildings and future research directions. Nat Hazard Rev 24(2):03123001
Mondoro A, Frangopol DM, Soliman M (2017) Optimal risk-based management of coastal bridges vulnerable to hurricanes. J Infrastruct Syst 23(3):04016046
Morison JR, Johnson JW, Schaaf SA (1950) The force exerted by surface waves on piles. J Petrol Technol 2(05):149–154
Mousavi ME, Irish JL, Frey AE, Olivera F, Edge BL (2011) Global warming and hurricanes: the potential impact of hurricane intensification and sea level rise on coastal flooding. Clim Change 104:575–597
Peng S, Qin X, Wang X, Huang G, Xiong X (2023) Experimental study of piezoelectric control for changing tilting pad journal bearing circumferential angle and radial displacement. Lubricants 11(12):510
Porter K, Kennedy R, Bachman R (2007) Creating fragility functions for performance-based earthquake engineering. Earthq Spectra 23(2):471–489
Qu K, Yao W, Tang HS, Agrawal A, Shields G, Chien SI et al (2021) Extreme storm surges and waves and vulnerability of coastal bridges in New York City metropolitan region: an assessment based on Hurricane Sandy. Nat Hazards 105:2697–2734

Rahman J, Billah AM (2023) Development of performance-based fragility curves of coastal bridges subjected to extreme wave-induced loads. J Bridg Eng 28(3):04023005
Rezende RC, Greco M, Lalo DF (2020) Numerical analysis of an elastomeric bearing pad by hyperelastic models. Rev Constr 19(3):301–310
Roeder CW, Stanton JF, Taylor AW (1987) Performance of elastomeric bearings (No. 298)
Saeidpour A, Chorzepa MG, Christian J, Durham S (2019) Probabilistic hurricane risk analysis of coastal bridges incorporating extreme wave statistics. Eng Struct 182:379–390
Shepherd TG (2008) Dynamics, stratospheric ozone, and climate change. Atmosphere-Ocean 46(1):117–138
Shoji G, Moriyama T (2007) Evaluation of the structural fragility of a bridge structure subjected to a tsunami wave load. J Nat Dis Sci 29(2):73–81
Tomiczek T, Wyman A, Park H, Cox DT (2019) Modified Goda equations to predict pressure distribution and horizontal forces for design of elevated coastal structures. J Waterw Port Coast Ocean Eng 145(6):04019023
Treloar LG (1975) The physics of rubber elasticity
Valanis KC (1971) A theory of viscoplasticity without a yield surface, part i: general theory. Arch Mech 23(4):517–533
Van De Lindt JW, Dao TN (2009) Performance-based wind engineering for wood-frame buildings. J Struct Eng 135(2):169–177. https://doi.org/10.1061/(asce)0733-9445(2009)135:2(169)
Van De Lindt JW, Taggart M (2009) Fragility analysis methodology for performance-based analysis of wood-frame buildings for flood. Nat Hazards Rev 10(3):113–123. https://doi.org/10.1061/(asce)1527-6988(2009)10:3(113)
Wen YK (1976) Method for random vibration of hysteretic systems. J Eng Mech Div 102(2):249–263
Xiang N, Li J (2016) Seismic performance of highway bridges with different transverse unseating-prevention devices. J Bridg Eng 21(9):04016045
Xiang N, Li J (2018) Effect of exterior concrete shear keys on the seismic performance of laminated rubber bearing-supported highway bridges in China. Soil Dyn Earthq Eng 112:185–197
Xiang N, Goto Y, Alam MS, Li J (2021) Effect of bonding or unbonding on seismic behavior of bridge elastomeric bearings: lessons learned from past earthquakes in China and Japan and inspirations for future design. Adv Bridge Eng 2:1–17
Xu Y, Xu G, Xue S, Wang J, Li Y (2022) Failure mechanism and vulnerability assessment of coastal box-girder bridge with laminated rubber bearings under extreme waves. Ocean Eng 266:112834
Yazdani N, Eddy S, & Cai CS (2000) Effect of bearing pads on precast prestressed concrete bridges. J Bridge Eng 5(3):224–232

Publisher's Note